Nodeless superconductivity and preserved time-reversal symmetry in the noncentrosymmetric Mo₃P superconductor

T. Shang,[1,*] J. Philippe,[2] J. A. T. Verezhak,[3] Z. Guguchia,[3] J. Z. Zhao,[4] L.-J. Chang,[5] M. K. Lee,[5] D. J. Gawryluk,[1,†]
E. Pomjakushina,[1] M. Shi,[6] M. Medarde,[1] H.-R. Ott,[2,7] and T. Shiroka[2,7]

[1]*Laboratory for Multiscale Materials Experiments, Paul Scherrer Institut, Villigen CH-5232, Switzerland*
[2]*Laboratorium für Festkörperphysik, ETH Zürich, CH-8093 Zurich, Switzerland*
[3]*Laboratory for Muon-Spin Spectroscopy, Paul Scherrer Institut, CH-5232 Villigen PSI, Switzerland*
[4]*Co-Innovation Center for New Energetic Materials, Southwest University of Science and Technology,
Mianyang 621010, People's Republic of China*
[5]*Department of Physics, National Cheng Kung University, Tainan 70101, Taiwan*
[6]*Swiss Light Source, Paul Scherrer Institut, Villigen CH-5232, Switzerland*
[7]*Paul Scherrer Institut, CH-5232 Villigen PSI, Switzerland*

We report a comprehensive study of the noncentrosymmetric superconductor Mo₃P. Its bulk superconductivity, with $T_c = 5.5$ K, was characterized via electrical-resistivity, magnetization, and heat-capacity measurements, while its microscopic electronic properties were investigated by means of muon-spin rotation/relaxation (μSR) and nuclear magnetic resonance (NMR) techniques. In the normal state, NMR relaxation data indicate an almost ideal metallic behavior, confirmed by band-structure calculations, which suggest a relatively high electron density of states, dominated by the Mo $4d$ orbitals. The low-temperature superfluid density, determined via transverse-field μSR and electronic specific heat, suggest a fully gapped superconducting state in Mo₃P, with zero-temperature gap $\Delta_0 = 0.83$ meV, the same as the BCS gap value in the weak-coupling case, and a zero-temperature magnetic penetration depth $\lambda_0 = 126$ nm. The absence of spontaneous magnetic fields below the onset of superconductivity, as determined from zero-field μSR measurements, indicates a preserved time-reversal symmetry in the superconducting state of Mo₃P and, hence, spin-singlet pairing.

I. INTRODUCTION

Noncentrosymmetric superconductors (NCSCs) belong to a class of materials that miss a key symmetry, such as parity [1]. In NCSCs the lack of inversion symmetry of the crystal lattice often induces an antisymmetric spin-orbit coupling (ASOC), which lifts the degeneracy of the conduction-band electrons and splits the Fermi surface. Consequently, both intra- and interband Cooper pairs can be formed. The admixture of spin-singlet and spin-triplet pairing in NCSCs is determined by the strength of the ASOC and by other microscopic parameters [1,2]. Cooper pairs with a spin-triplet pairing have a nonzero spin, which implies a weak magnetic moment in the superconducting state and a breaking of the time-reversal symmetry (TRS). This is the case of, e.g., Sr₂RuO₄ and UPt₃, known to exhibit triplet superconductivity [3–6], and where the TRS breaking in the SC state has been confirmed by measurements of both zero-field muon-spin relaxation/rotation (μSR) and the polar Kerr effect [7–10].

Some NCSCs are known to show a broken TRS upon the onset of superconductivity. Examples include LaNiC₂ [11],

La₇Ir₃ [12], and some Re-based binary alloys ReT ($T =$ transition metal, e.g., Ti, Zr, Nb, Hf) [13–16]. In the weak-SOC limit, TRS breaking can be achieved via nonunitary triplet pairing, such as in noncentrosymmetric LaNiC₂ [11,17] and centrosymmetric LaNiGa₂ [18,19]. In the case of ReT alloys, where a strong SOC is present, the T_d point group has several irreducible representations with dimension larger than 1. Therefore, they can support TRS breaking with singlet, triplet, or admixed pairings. For ReT, there are a number of possible TRS-breaking states [16]; however, all such states have symmetry-constrained point or line nodes in the gap, inconsistent with the experimentally observed nodeless gap [13–16]. To explain a fully gapped superconducting state exhibiting broken TRS, a model employing loop Josephson currents (LJCs) was recently proposed [20]. This model is based on an on-site, intraorbital, singlet-pairing SC state, where a phase shift among the on-site singlet pairs gives rise to the LJCs within a unit cell. Such currents can produce weak internal magnetic fields, which break the TRS and can, in principle, be detected experimentally.

Despite numerous examples of NCSCs, to date only a few of them are known to break TRS in their superconducting state. The causes of such a selective TRS breaking remain largely unknown. Consequently, comprehensive studies of other NCSCs, such as Mo₃P reported here, may help to identify the origin of this behavior. Superconductivity in

---

*Corresponding author: tian.shang@psi.ch
†On leave from Institute of Physics, Polish Academy of Sciences, Aleja Lotnikow 32/46, PL-02-668 Warsaw, Poland.

Mo$_3$P was first reported in 1954 [21] and confirmed ten years later [22]. In that same year, also the Mo$_3$P crystal structure was determined [23]. To our knowledge, none of these early works had a follow-up regarding the characterization of the superconducting properties of Mo$_3$P.

In this paper, we report on an extensive study of the Mo$_3$P physical properties, in both the normal and superconducting state, by means of electrical-resistivity, magnetization, thermodynamic, muon-spin relaxation (μSR), and nuclear magnetic resonance (NMR) methods. In addition, we also present theoretical density functional theory (DFT) band-structure calculations. Despite a noncentrosymmetric crystal structure, Mo$_3$P is shown to be a moderately correlated electron material, which adopts a fully gapped, spin-singlet superconducting state with preserved TRS.

II. EXPERIMENTAL DETAILS

Polycrystalline samples of Mo$_3$P were prepared via solid-state reaction, where high-purity (99.999%) Mo powders and P pieces were mixed in a stoichiometric ratio and made to react at 1100°C for 48 hours. The resulting powders were thoroughly grounded and pressed into pellets and then sintered at 1100°C for over 48 hours. The final product had a silvery color, indicative of good metallicity. Room-temperature x-ray powder diffraction (XRD) measurements were performed by using a Bruker D8 diffractometer with Cu Kα radiation. The magnetic-susceptibility, electrical resistivity, and specific-heat measurements were performed on a 7 T Quantum Design magnetic property measurement system (MPMS-7) and a 14 T physical property measurement system (PPMS-14) equipped with a dilution refrigerator (DR). The μSR measurements were carried out at the GPS and HAL-9500 spectrometers of the Swiss muon source at Paul Scherrer Institut, Villigen, Switzerland [24]. For the low-temperature HAL measurements, the samples were mounted on a silver plate using diluted GE varnish. The μSR data were analyzed by means of the MUSRFIT software package [25].

The ^{31}P NMR measurements, including line shapes and spin-lattice relaxation times, were performed on Mo$_3$P powder in two external magnetic fields, 0.503 and 7.067 T. This allowed us to compare the NMR parameters in the superconducting and the normal state, respectively. The NMR signals were monitored by means of standard spin-echo sequences, consisting of $\pi/2$ and π pulses of 2.7 and 5.4 μs, with recycling delays ranging from 0.25 to 20 s, in a temperature range 1.95 to 295 K. The line shapes were obtained via fast Fourier transform (FFT) of the echo signal. Spin-lattice relaxation times T_1 were measured via the inversion recovery method, using a π-$\pi/2$-π pulse sequence.

The electronic structure of Mo$_3$P was calculated by using the full-potential linearized augmented plane-wave (LAPW) method, as implemented in the WIEN2k package [26]. In particular, we employed the generalized gradient approximation (GGA) [27]. The Brillouin zone integration was performed on a regular mesh of $10 \times 10 \times 10$ points. Muffin-tin radii (r_{mt}) of 2.41 and 2.06 r_{Bohr} were chosen for Mo and P atoms, respectively. The largest plane-wave vector was defined by $r_{mt}k_{max} = 8$. The SOC was treated by using a second-order variational procedure [26].
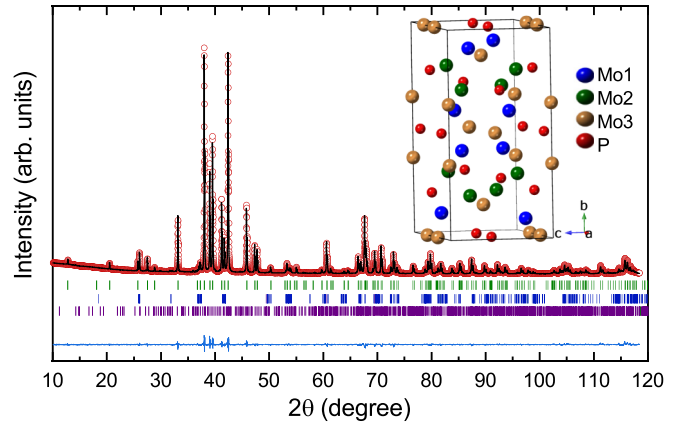

FIG. 1. Room-temperature x-ray powder diffraction pattern and Rietveld refinement for Mo$_3$P. The open red circles and the solid black line represent the experimental pattern and the Rietveld-refinement profile, respectively. The blue line at the bottom shows the residuals, i.e., the difference between calculated and experimental data. The vertical bars mark the calculated Bragg-peak positions for Mo$_3$P (green), MoO$_2$ (blue), and Mo$_3$P$_4$ (purple). The crystal structure (unit cell) is shown in the inset.

III. RESULTS AND DISCUSSION

A. Crystal structure

The crystal structure and the purity of Mo$_3$P polycrystalline samples were checked via XRD at room temperature. Figure 1 shows a representative XRD pattern, analyzed by means of the FullProf Rietveld-analysis suite [28]. As previously reported [23], we confirm that Mo$_3$P crystallizes in the tetragonal noncentrosymmetric α-V$_3$S-type structure with space group $I\bar{4}2m$ (No. 121). The refined lattice parameters, $a = b = 9.79094(2)$ Å and $c = 4.826099(13)$ Å, are consistent with the reported values, but here established with a substantially improved accuracy. According to the refinements in Fig. 1, tiny amounts of Mo$_4$P$_3$ (3.46%) and MoO$_2$ (4.28%) phases were also identified. The refined Mo$_3$P crystal structure, shown in the inset, comprises three different Mo sites and a single P site in the unit cell. Table I summarizes the atomic positions and the lattice parameters.

B. Electrical resistivity

The temperature-dependent electrical resistivity $\rho(T)$ of Mo$_3$P was measured from room temperature down to 2 K. As shown in Fig. 2, the resistivity data reveal a metallic behavior down to the superconducting transition at T_c. No anomalies associated with structural, magnetic, or charge-density-wave transitions could be detected. The electrical resistivity in the low-temperature region is shown in the inset, where the superconducting transition (with $T_c^{onset} = 5.7$ K and $T_c^{zero} = 5.5$ K) is clearly seen. The $\rho(T)$ curve below 300 K can be described by the Bloch-Grüneisen-Mott (BGM) formula [29,30]:

$$\rho(T) = \rho_0 + 4A\left(\frac{T}{\Theta_D^R}\right)^5 \int_0^{\frac{\Theta_D^R}{T}} \frac{z^2 dz}{(e^z - 1)(1 - e^{-z})} - \alpha T^3.$$

(1)

TABLE I. Refined Mo_3P crystal-lattice parameters and atomic coordinates, as determined at room temperature. Z represents the number of formula units in the unit cell.

Parameter	Value
Structure	tetragonal, α-V_3S type
Space group	$I\bar{4}2m$ (No. 121)
Z	8
a (Å)	9.79094(2)
c (Å)	4.826099(13)
V_{cell} (Å^3)	462.6419(19)
R_p	2.65%
R_{wp}	3.70%
R_{exp}	1.14%
χ_r^2	10.5

		Atomic Coordinates			
Atom	Wyckoff	Occ.	x	y	z
P	$8f$	0.5	0.2924(3)	0	0
Mo_1	$8g$	0.5	0.35541(9)	0	0.5
Mo_2	$8i$	0.5	0.09289(7)	0.09289(7)	0.2657(3)
Mo_3	$8i$	0.5	0.29871(7)	0.29871(7)	0.2649(3)

Here the first term ρ_0 is the residual resistivity due to the scattering of conduction electrons on the static defects of the crystal lattice, while the second term describes the electron-phonon scattering, with Θ_D^R being the characteristic (Debye) temperature and A a coupling constant. The third term represents a contribution due to s-d interband scattering, α being the Mott coefficient [31,32]. The fit in Fig. 2 (gray line) results in $\rho_0 = 5.92(5)$ $\mu\Omega$ cm, $A = 300(7)$ $\mu\Omega$ cm, $\Theta_D^R = 251(3)$ K, and $\alpha = 3.4(1) \times 10^{-6}$ $\mu\Omega$ cm K^{-3}. The fairly large residual resistivity ratio (RRR), i.e., $\rho(300$ K$)/\rho_0 \sim 45$, and the sharp superconducting transition ($\Delta T = 0.2$ K) both indicate a good sample quality.
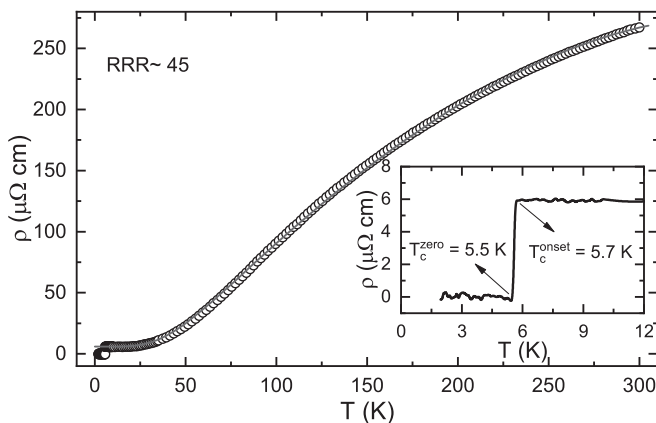

FIG. 2. Temperature dependence of the Mo_3P electrical resistivity. The solid gray line through the data is a fit to Eq. (1). The inset shows the enlarged low-temperature data region, highlighting the superconducting transition.
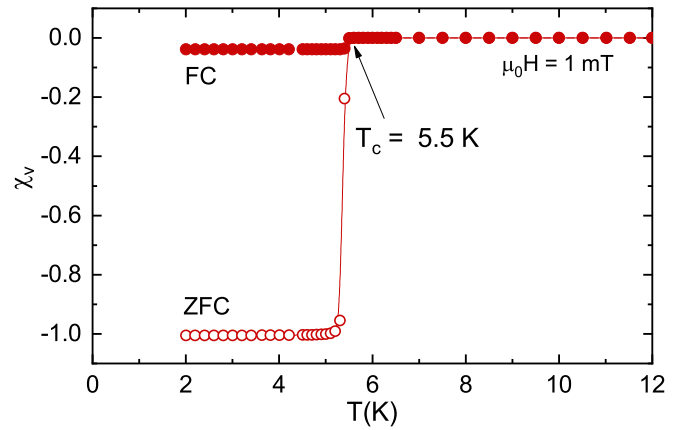

FIG. 3. Temperature dependence of the Mo_3P magnetic susceptibility χ_v ($\equiv \chi$), measured using ZFC and FC protocols. Data were collected in a 1 mT applied field in a 1.8–12 K temperature range.

C. Magnetic susceptibility

The superconductivity of Mo_3P was also probed by magnetic susceptibility measurements. The temperature dependence of the magnetic susceptibility $\chi(T)$ was determined using both field-cooled (FC) and zero-field-cooled (ZFC) protocols in an applied field of 1 mT. As shown in Fig. 3, $\chi(T)$ data show a superconducting transition at $T_c = 5.5$ K, consistent with the values determined from electrical resistivity (Fig. 2) and heat capacity (see below). The splitting of the FC and ZFC susceptibilities is a typical feature of type-II superconductors with moderate to strong pinning, where the magnetic-field flux is pinned upon cooling the material in an applied field. Below T_c, a ZFC-susceptibility value of $\chi_v \sim -1$ (after accounting for demagnetization factor, powder compactness, etc.) indicates bulk superconductivity.

D. Lower and upper critical fields

To determine the lower critical field μ_0H_{c1} of Mo_3P, its field-dependent magnetization $M(H)$ was measured at various temperatures up to T_c, as shown in Fig. 4(a). The $M(H)$ curves, recorded using a ZFC-protocol, show the typical response of a type-II superconductor. The estimated μ_0H_{c1} values at different temperatures, determined from the deviation of $M(H)$ from linearity, are plotted in Fig. 4(b). The solid line is a fit to $\mu_0H_{c1}(T) = \mu_0H_{c1}(0)[1 - (T/T_c)^2]$. This provides a lower critical field $\mu_0H_{c1}(0) = 29.4(2)$ mT, consistent with 24.9(5) mT, the value calculated from the magnetic penetration depth λ_0 (see below).

To investigate the behavior of the upper critical field μ_0H_{c2}, we measured the temperature-dependent electrical resistivity $\rho(T)$ and specific heat $C(T)/T$ at various applied magnetic fields, as well as the field-dependent magnetization $M(H)$ at various temperatures up to T_c. As shown in Figs. 5(a) and 5(b), the superconducting transition, determined from $\rho(T)$ and specific-heat $C(T)/T$ data, shifts towards lower temperature upon increasing the magnetic field. In zero magnetic field, $T_c = 5.5$ K determined from $C(T)/T$ is consistent with the T_c values determined from $\rho(T)$ (Fig. 2) and $\chi(T)$ (Fig. 3) data. In the latter case, as shown in Fig. 5(c), the diamagnetic signal disappears once the applied magnetic
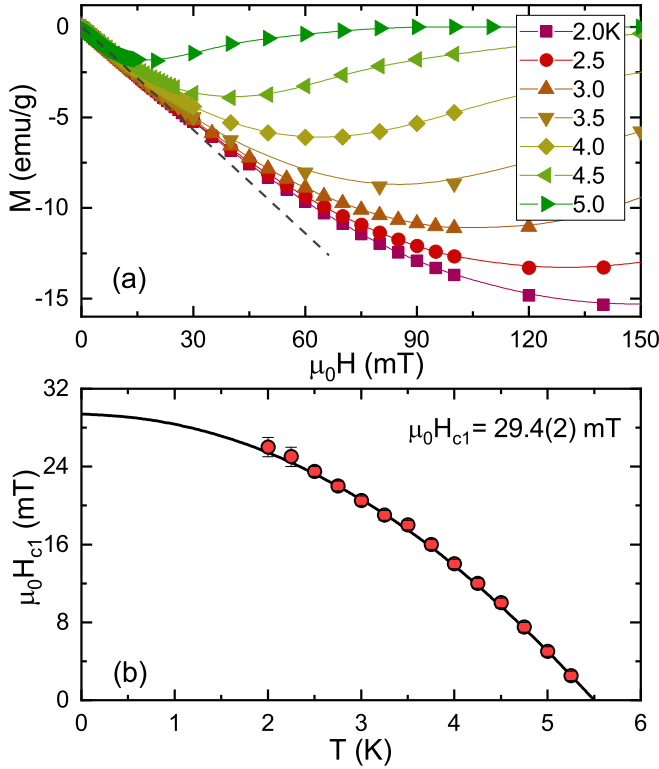
FIG. 4. (a) Field-dependent magnetization $M(H)$ recorded at various temperatures up to T_c. For each temperature, the lower critical field $\mu_0 H_{c1}$ was determined as the value at which $M(H)$ deviates from linearity (dashed line). (b) Estimated lower critical field $\mu_0 H_{c1}$ as a function of temperature, with the solid line representing a fit to $\mu_0 H_{c1}(T) = \mu_0 H_{c1}(0)[1 - (T/T_c)^2]$.
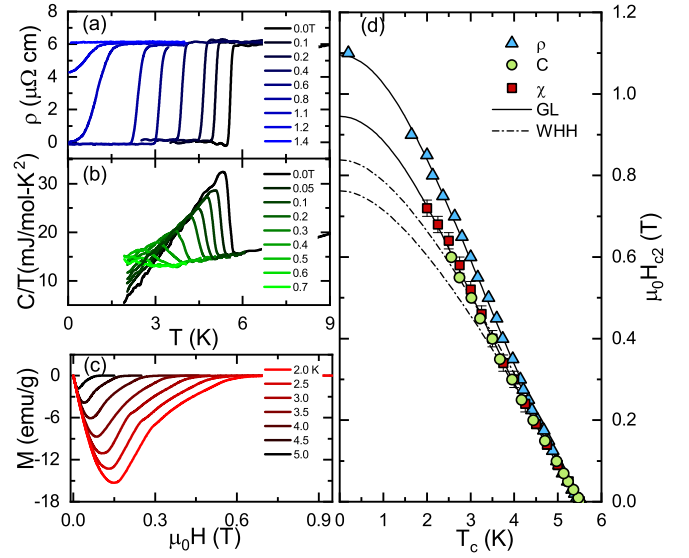

FIG. 5. Temperature-dependent electrical resistivity $\rho(T, H)$ (a) and specific heat $C/T(T, H)$ (b) for different applied magnetic fields, up to 1.4 T. In the first case, T_c was defined as the onset of zero resistance. (c) Field-dependent magnetization $M(H, T)$ measured at various temperatures and in applied magnetic fields up to 1.0 T. From $\rho(T, H)$, $C(T, H)/T$, and $M(H, T)$ one can derive the upper critical field $\mu_0 H_{c2}$, as shown in (d). The solid lines represent fits to an effective GL model, whereas the dash-dotted lines are fits based on a WHH model without spin-orbit scattering.

field exceeds the upper critical field. Figure 5(d) summarizes the upper critical fields vs the superconducting transition temperatures T_c, as derived from $\rho(T, H)$, $C(T, H)/T$, and $M(H, T)$ data, respectively. The temperature dependence of $\mu_0 H_{c2}(T)$ was analyzed by means of the semiempirical model $\mu_0 H_{c2}(T) = \mu_0 H_{c2}(0)(1 - t^2)/(1 + t^2)$, where $t = T/T_c$ is the normalized temperature (see, e.g., [33]). This model follows from the Ginzburg-Landau (GL) relation between H_{c2} and the coherence length ξ (see below), by assuming $\xi(t) \propto \sqrt{(1 + t^2)/(1 - t^2)}$. Although the GL theory is strictly valid near T_c, the above form of $H_{c2}(T)$ has been shown to be satisfied in a wider temperature range. The solid lines in Fig. 5(d) are fits to the GL model, which gives $\mu_0 H_{c2}^{\mathrm{GL}}(0) = 0.94(1)$ T and 1.09 T for specific-heat and magnetization data and for electrical-resistivity data, respectively. For a comparison, we estimated the upper critical field also by means of the Werthamer-Helfand-Hohenberg (WHH) model [34]. The dashed-lines in Fig. 5(d) are fits to a WHH model without spin-orbit scattering and give $\mu_0 H_{c2}^{\mathrm{WHH}}(0) = 0.76(1)$ T and 0.83(1) T for specific-heat and magnetization data and for electrical-resistivity data, respectively.

At low fields, both GL and WHH models describe the experimental data very well. At higher applied fields, however, the WHH-type fits deviate significantly from the data, clearly providing underestimated critical-field values. The remarkable agreement of the less elaborate GL model with ex-

perimental data is clearly seen in Fig. 5(d). We note that while the specific-heat, magnetization, and electrical-resistivity data sets agree well at low fields (<0.25 T), at higher fields, the transition temperatures determined from $\rho(T, H)$ are systematically higher than those derived from $C(T, H)/T$ and $M(H, T)$ data. A similar behavior has also been found in other NCSCs, e.g., LaPtSi, BiPd, or LaTSi$_3$ ($T = $ Pd, Pt, and Ir) [35–39], as well as in standard superconductors. Generally, the surface/filamentary superconductivity above bulk T_c, or a strong anisotropy of the upper critical field, is proposed as the cause of the differing T_c values. In order to clarify this issue, studies of single-crystal specimens are highly desirable.

In the GL theory of superconductivity, the coherence length ξ can be calculated from $\xi = \sqrt{\Phi_0/2\pi H_{c2}}$, where $\Phi_0 = 2.07 \times 10^{-3}$ T μm^2 is the quantum of magnetic flux. With a bulk $\mu_0 H_{c2}(0) = 0.94(1)$ T, the calculated $\xi(0)$ is 18.7(1) nm. The magnetic penetration depth λ is related to the coherence length ξ and the lower critical field $\mu_0 H_{c1}$ via $\mu_0 H_{c1} = (\Phi_0/4\pi\lambda^2)[\ln(\kappa) + 0.5]$, where $\kappa = \lambda/\xi$ is the GL parameter [40]. By using $\mu_0 H_{c1} = 29.4$ mT and $\xi = 18.7$ nm, the resulting magnetic penetration depth $\lambda_{\mathrm{GL}} = 113(1)$ nm is consistent with 126(1) (zero-field extrapolation) and 121(2) nm (50 mT), the experimental values from TF-μSR data (see Sec. III F and Table II). A GL parameter $\kappa \sim 7$, almost ten times larger than the $1/\sqrt{2}$ threshold value, clearly confirms that Mo$_3$P is a type-II superconductor.

E. Zero-field specific heat

Specific-heat data offer valuable insight into the superconducting properties, including the gap value and its symmetry.

TABLE II. Normal- and superconducting-state properties of Mo_3P, as determined from electrical-resistivity, magnetic-susceptibility, specific-heat, NMR, and μSR measurements. The London penetration depth λ_L, effective mass $m^\star$, bare band-structure effective mass $m^\star_{band}$, carrier density n_s, BCS coherence length ξ_0, electronic mean-free path l_e, Fermi velocity v_F, and effective Fermi temperature T_F were estimated following Eqs. (40)–(50) in Ref. [65].

Property	Unit	Value
T_c [a]	K	5.5(2)
ρ_0	$\mu\Omega$ cm	5.92(5)
Θ_D^R	K	251(2)
$\mu_0 H_{c1}$	mT	29.4(2)
$\mu_0 H_{c1}^{\mu SR}$	mT	24.9(5)
$\mu_0 H_{c2}^\rho$	T	1.09(1)
$\mu_0 H_{c2}^{\chi,C}$	T	0.94(1)
$\mu_0 H_{c2}^{\mu SR}$	T	0.96(3)
$\xi(0)$	nm	18.7(1)
γ_n	mJ/(mol K^2)	10.3(4)
Θ_D^C	K	225(3)
λ_{ep}		0.72(1)
$N(\epsilon_F)$	states/(eV f.u.)	2.2(1)
$N_{band}(\epsilon_F)$	states/(eV f.u.)	1.28(1)
$N(\epsilon_F)^{DFT}$	states/(eV f.u.)	1.56
E_{ASOC}	meV	90
$\Delta_0^{\mu SR}$	meV	0.83(1)
Δ_0^C	meV	0.82(1)
$\Delta C/\gamma_n T_c$		1.44(1)
λ_0 [b]	nm	126(1)
λ_0	nm	121(2)
λ_{GL}	nm	113(1)
λ_L	nm	63(1)
$m^\star$	m_e	5.4(2)
m_{band}	m_e	3.1(2)
n_s	10^{28} m^{-3}	3.86(3)
ξ_0	nm	56 (1)
l_e	nm	18.8(2)
v_F	10^5 ms^{-1}	2.22(7)
T_F	10^4 K	1.78(6)

[a]Similar values were determined via electrical resistivity, magnetic susceptibility, and heat-capacity measurements.

[b]Derived from a fit to Eq. (8).

Therefore, the Mo_3P specific heat was measured down to 0.1 K in zero field. As shown in Fig. 6, there is a clear specific-heat jump at T_c, indicating a bulk superconducting transition. The electronic specific heat C_e/T was obtained by subtracting the phonon contribution from the experimental data. As shown in the inset of Fig. 6, the normal-state specific heat of Mo_3P is fitted to $C/T = \gamma_n + \beta T^2$, where γ_n is the electronic specific heat coefficient and βT^2 is the phonon contribution to the specific heat. The derived values are $\gamma_n = 10.3(4)$ mJ/(mol K^2) and $\beta = 0.67(3)$ mJ/(mol K^4). The Debye temperature Θ_D^C can be calculated by using $\Theta_D^C = (12\pi^4 Rn/5\beta)^{1/3}$, where $R = 8.314$ J/(mol K) is the molar gas constant and $n = 4$ is the number of atoms per formula unit. The resulting $\Theta_D^C = 225(3)$ K (extracted from low-T data) is consistent with the value derived from electrical-resistivity data (see Fig. 2). The density of states (DOS) at the Fermi level $N(\epsilon_F)$ was evaluated from the expression $N(\epsilon_F) = 3\gamma_n/(2\pi^2 k_B^2) = 2.2(1)$
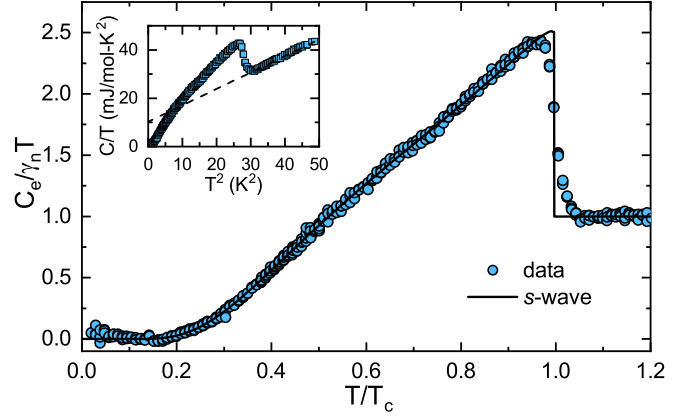

FIG. 6. Normalized electronic specific heat $C_e/\gamma_n T$ for Mo_3P versus T/T_c. Inset: The measured specific heat C/T as a function of T^2. The dashed line in the inset is a fit to $C/T = \gamma + \beta T^2$, while the solid line in the main panel is the electronic specific heat calculated by considering a fully gapped s-wave model.

states/(eV f.u.) (accounting for spin degeneracy) [41], where k_B is the Boltzmann constant. The electron-phonon coupling constant λ_{ep}, a measure of the attractive interaction between electrons due to phonons, was estimated from the Θ_D^C and T_c values by applying the semiempirical McMillan formula [42]:

$$\lambda_{ep} = \frac{1.04 + \mu^\star \ln(\Theta_D/1.45T_c)}{(1 - 0.62\,\mu^\star)\ln(\Theta_D/1.45T_c) - 1.04}. \quad (2)$$

The Coulomb pseudopotential $\mu^\star$, usually lying in the 0.09–0.18 range, was here fixed to 0.13, a commonly used value for transition metals. From Eq. (2) we obtain $\lambda_{ep} = 0.72(1)$ for Mo_3P, almost twice the reported value for the elemental Mo (0.41) [43,44]. Finally, the band-structure density of states $N_{band}(\epsilon_F)$ can be estimated from the relation $N_{band}(\epsilon_F) = N(\epsilon_F)/(1 + \lambda_{ep})$ [41], which gives $N_{band}(\epsilon_F) = 1.28(1)$ states/(eV f.u.).

The electronic specific heat divided by the electronic specific heat coefficient, i.e., $C_e/\gamma_n T$, is shown in the main panel of Fig. 6 as a function of the reduced temperature. The temperature-independent behavior of $C_e/\gamma_n T$ at low T suggests a fully gapped superconducting state in Mo_3P. The temperature-dependent superconducting-phase contribution to the entropy was calculated by means of [45]

$$S(T) = -\frac{6\gamma_n}{\pi^2 k_B} \int_0^\infty [f\ln f + (1-f)\ln(1-f)]\,d\epsilon, \quad (3)$$

where $f = (1 + e^{E/k_B T})^{-1}$ is the Fermi function, Δ_0 is the SC gap value at 0 K, and $E(\epsilon) = \sqrt{\epsilon^2 + \Delta^2(T)}$ is the excitation energy of quasiparticles, with ϵ the electron energies measured relative to the chemical potential (Fermi energy) [45,46]. $\Delta(T)$ is the same as in Sec. III F. The temperature-dependent electronic specific heat in the superconducting state can be calculated from $C_e = T\frac{dS}{dT}$. The solid line in Fig. 6 represents a fit with a fully gapped s-wave model. The resulting superconducting gap $\Delta_0 = 0.82(1)$ meV is consistent with the μSR results (see Fig. 9). The Mo_3P gap value Δ_0, as derived from both specific-heat and TF-μSR data, is comparable to the expected weak-coupling BCS value 0.80 meV, thus indicating weakly coupled superconducting
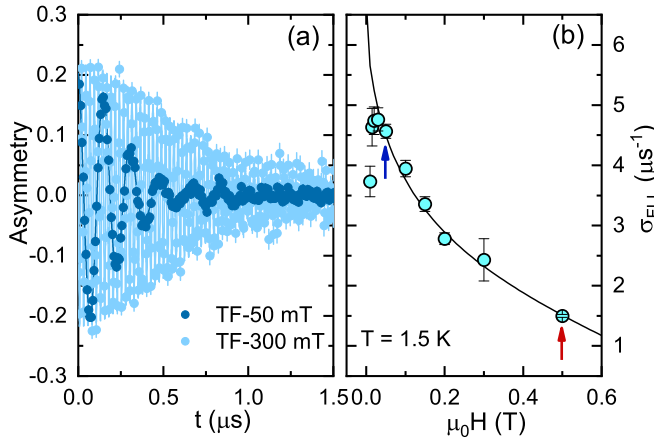
FIG. 7. (a) Time-domain TF-μSR spectra of Mo_3P measured in its superconducting state (at $T = 1.5$ K) at 50 and 300 mT. (b) Field-dependent Gaussian relaxation rate $\sigma_{FLL}(H)$. The arrows indicate the field values (50 and 500 mT) used in the temperature-dependent TF-μSR studies. The solid line is a fit to Eq. (8).

pairs in Mo_3P. Furthermore, also the specific-heat discontinuity at T_c, i.e., $\Delta C/\gamma_n T_c = 1.44$, is fully consistent with the conventional BCS of 1.43.

F. Transverse-field μSR

To investigate the superconducting properties of Mo_3P at a microscopic level, we carried out μSR measurements in applied transverse fields (TFs). The optimal field value for such experiments was determined via a preliminary field-dependent μSR depolarization-rate measurement at 1.5 K. To track the additional field-distribution broadening due to the flux-line lattice (FLL) in the mixed superconducting state, a magnetic field (up to 500 mT) was applied in the normal state and then the sample was cooled down to 1.5 K. Figure 7(a) shows the TF spectra in an applied field of 50 and 300 mT, respectively. The solid lines represent fits using the same model as described in Eq. (4) below. The resulting Gaussian relaxation rate $\sigma_{FLL}(H)$ is summarized in Fig. 7(b). Above the lower critical field $\mu_0 H_{c1}$ (29.4 mT), the relaxation rate decreases continuously. By considering the decrease of the intervortex distance with the field and the vortex-core effects, a field of 50 mT was chosen for the temperature-dependent TF-μSR studies. For a comparison, the TF-μSR relaxation was also measured in a field of 500 mT. The field dependence of the Gaussian relaxation rate was analyzed following Eq. (8) (see details below). The derived zero-temperature $\mu_0 H_{c2} = 0.96(1)$ T and magnetic penetration depth $\lambda_0 = 126(1)$ nm are consistent with the temperature-dependent 50 mT results (see Table II).

The TF-μSR time spectra were collected at various temperatures up to T_c, following a field-cooling protocol on both GPS and HAL instruments. Figures 8(a) and 8(b) show two representative TF-μSR spectra collected above (7.5 K) and below T_c (1.5 K) on GPS. The enhanced depolarization rate below T_c reflects the inhomogeneous field distribution due to the FLL, which causes the additional distribution broadening in the mixed state [see Fig. 8(c)]. The time evolution of the
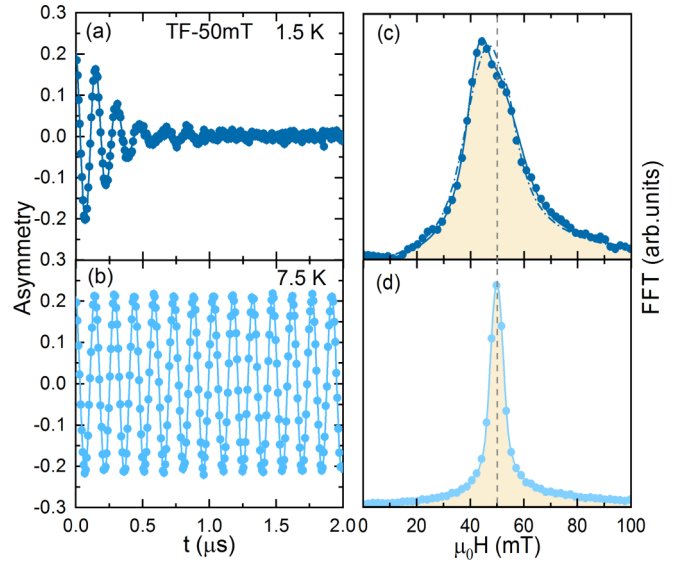

FIG. 8. TF-μSR time-dependent spectra, collected at 1.5 K (a) and 7.5 K (b) in an applied field of 50 mT. Fourier transforms of the above time spectra at 1.5 K (c) and 7.5 K (d). The solid lines are fits to Eq. (4) using two oscillations, while the dash-dotted line in (c) represents a fit with a single oscillation. The vertical dashed line indicates the applied magnetic field. Note the clear diamagnetic shift below T_c in (c).

μSR asymmetry can be modeled by

$$A_{TF}(t) = \sum_{i=1}^{n} A_i \cos(\gamma_\mu B_i t + \phi)e^{-\sigma_i^2 t^2/2}$$
$$+ A_{bg}\cos(\gamma_\mu B_{bg}t + \phi). \quad (4)$$

Here A_i and A_{bg} represent the initial muon-spin asymmetries for muons implanted in the sample and sample holder, respectively, with the latter not undergoing any depolarization. B_i and B_{bg} are the local fields sensed by implanted muons in the sample and sample holder, $\gamma_\mu = 2\pi \times 135.53$ MHz/T is the muon gyromagnetic ratio, ϕ is the shared initial phase, and σ_i is a Gaussian relaxation rate of the ith component. The number of required components is material dependent, generally in the $1 \leqslant n \leqslant 5$ range. For superconductors with a large κ ($\gg 1$) value, the magnetic penetration depth is much larger than the coherence length. Hence, the field distribution is narrow and a single-oscillating component is sufficient to describe $A(t)$. In case of a small κ ($\gtrsim 1/\sqrt{2}$) value, the magnetic penetration depth is comparable to the coherence length. This implies a broad field distribution, in turn requiring multiple oscillations to describe $A(t)$.

Figures 8(c) and 8(d) show the FFT spectra of the TF-μSR time-domain asymmetries at 1.5 K and 7.5 K. Solid lines represent fits to Eq. (4) using two oscillations (i.e., $n = 2$) in the superconducting phase and one oscillation in the normal phase. In the 1.5 K case, a single-component oscillation [dash-dotted line in panel (c)] is clearly unable to fit the $T < T_c$ data. The derived Gaussian relaxation rates as a function of temperature are summarized in the insets of Fig. 9. Above T_c the relaxation rate is small and temperature independent, but below T_c it starts to increase due to the onset of the FLL
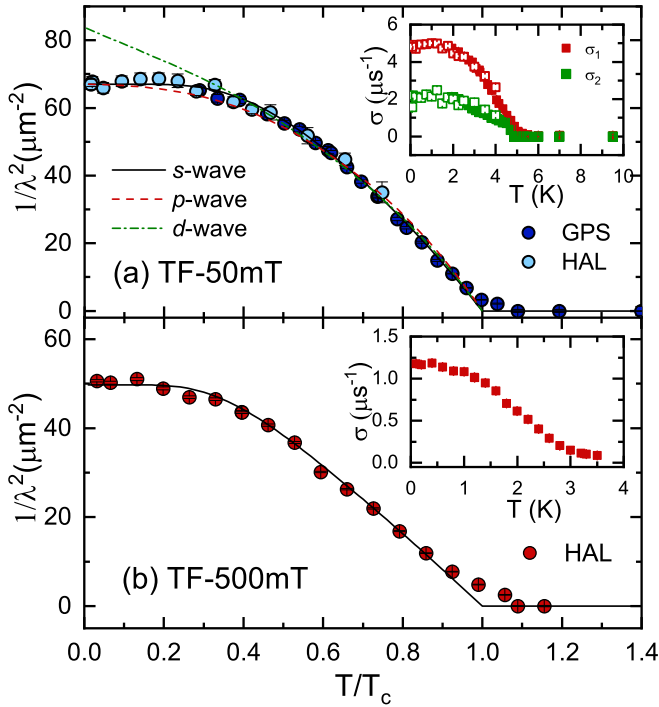
FIG. 9. Superfluid density vs temperature, as determined from TF-μSR measurements in an applied magnetic field of 50 mT (a) and 500 mT (b). The insets show the temperature dependence of the muon-spin relaxation rate $\sigma(T)$. Two components are required to describe the 50 mT experimental data [see details in Fig. 8(c)]. The different lines represent fits to various models, including s-, p-, and d-wave pairing (see text for details).

and the increase in superfluid density. Unlike the TF-μSR spectra collected at 50 mT, the 500 mT data sets can be described by a single oscillation. This reflects the narrower internal-field distribution for applied fields comparable to H_{c2}. In case of multicomponent oscillations (at 50 mT), the first-term in Eq. (4) describes the field distribution as the sum of n Gaussian relaxations [47]:

$$P(B) = \gamma_\mu \sum_{i=1}^{2} \frac{A_i}{\sigma_i} \exp\left[-\frac{\gamma_\mu^2 (B - B_i)^2}{2\sigma_i^2}\right]. \quad (5)$$

Then, the first and second moments of the field distribution in the sample were calculated by

$$\langle B \rangle = \sum_{i=1}^{2} \frac{A_i B_i}{A_{\text{tot}}}, \quad (6)$$

$$\langle B^2 \rangle = \frac{\sigma_{\text{eff}}^2}{\gamma_\mu^2} = \sum_{i=1}^{2} \frac{A_i}{A_{\text{tot}}} \left[\frac{\sigma_i^2}{\gamma_\mu^2} - (B_i - \langle B \rangle)^2\right], \quad (7)$$

where $A_{\text{tot}} = \sum_{i=1}^{2} A_i$. In the superconducting state, the measured Gaussian relaxation rate includes contributions from both a temperature-independent relaxation due to nuclear moments (σ_n) and the FLL (σ_{FLL}). The FLL-related relaxation can be extracted by subtracting the nuclear contribution according to $\sigma_{\text{FLL}} = \sqrt{\sigma_{\text{eff}}^2 - \sigma_n^2}$. Since σ_{FLL} is directly related to the magnetic penetration depth and the superfluid density

($\sigma_{\text{FLL}} \propto 1/\lambda^2$), the superconducting gap value and its symmetry can be determined from the measured $\sigma_{\text{FLL}}(T)$.

For small applied magnetic fields ($H_{\text{appl}}/H_{c2} \ll 1$) and large κ values ($\kappa \gg 1$), σ_{FLL} is field independent and proportional to λ^{-2} [40,48]. In the Mo$_3$P case, however, the upper critical field μH_{c2} is relatively small (0.94 T) compared to the applied TF field (50 and 500 mT). Therefore, to extract the penetration depth from the measured σ_{FLL}, the effects of overlapping vortex cores with increasing field have to be considered, requiring the following expression for calculating the magnetic penetration depth λ [40,48]:

$$\sigma_{\text{FLL}} = 0.172 \frac{\gamma_\mu \Phi_0}{2\pi} (1 - h)[1 + 1.21(1 - \sqrt{h})^3]\lambda^{-2}, \quad (8)$$

where $h = H_{\text{appl}}/H_{c2}$, with H_{appl} the applied magnetic field. The above expression is valid for type-II superconductors with $\kappa \geqslant 5$ in the $0.25/\kappa^{1.3} \lesssim h \leqslant 1$ field range. With $\kappa \sim 6$ and $h = 0.053$ (TF 50 mT) and 0.53 (TF 500 mT), Mo$_3$P fulfills the above conditions.

By using Eq. (8), we could calculate the inverse square of the magnetic penetration depth, whose temperature dependence is shown in Fig. 9. To gain insight into the superconducting pairing symmetry in Mo$_3$P, the temperature-dependent superfluid density $\rho_{\text{sc}}(T)$ [$\lambda^{-2}(T) \propto \rho_s(T)$] was further analyzed by means of different models, generally described by

$$\rho_{\text{sc}}(T) = 1 + 2\left\langle \int_{\Delta_k}^{\infty} \frac{E}{\sqrt{E^2 - \Delta_k^2}} \frac{\partial f}{\partial E} dE \right\rangle_{\text{FS}}, \quad (9)$$

where Δ_k is an angle-dependent gap function, $f = (1 + e^{E/k_B T})^{-1}$ is the Fermi function, and $\langle \cdots \rangle_{\text{FS}}$ represents an average over the Fermi surface [45]. The gap function can be written as $\Delta_k(T) = \Delta(T)g_k$, where Δ is the maximum gap value and g_k is the angular dependence of the gap, equal to 1, $\cos 2\psi$, and $\sin \theta$ for an s-, d-, and p-wave model, respectively. Here ψ and θ are azimuthal angles. The temperature dependence of the gap is assumed to follow $\Delta(T) = \Delta_0 \tanh\{1.82[1.018(T_c/T - 1)]^{0.51}\}$ [49], where Δ_0, the gap value at zero temperature, is the only adjustable parameter. Note that the function $\Delta(T)$ is practically model independent.

Three different models, including s, d, and p waves, were used to describe the temperature-dependent superfluid density $\lambda^{-2}(T)$ measured in an applied field of 50 mT [Fig. 9(a)], with the first two being singlet pairing and the last one triplet pairing. For the s- and p-wave model, the estimated gap values are 0.83(1) and 1.12(1) meV, respectively, with the shared zero-temperature magnetic penetration depth $\lambda_0 = 121(2)$ nm, while for the d-wave model, the estimated λ_0 and gap values are 109(2) nm and 1.10(1) meV. As can be seen in Fig. 9(a), the temperature-independent behavior of $\lambda^{-2}(T)$ below $1/3 T_c$ strongly suggests a nodeless superconductivity in Mo$_3$P. Therefore, $\lambda^{-2}(T)$ is clearly more consistent with a single fully gapped s-wave model. In case of d- or p-wave models, a less-good agreement with the measured λ^{-2} values is found, especially at low temperature. Such conclusions are further supported by the low-T specific-heat data shown in Fig. 6. Also in the TF 500 mT case [see Fig. 9(b)], the $\lambda^{-2}(T)$ dependence is consistent with an s-wave model,
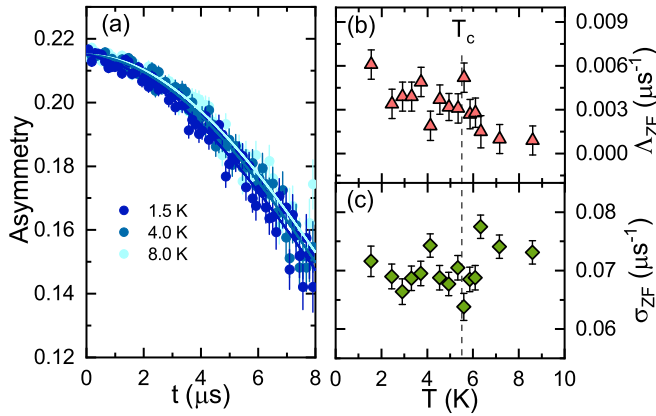
FIG. 10. (a) Representative ZF-μSR spectra for Mo$_3$P in the superconducting (1.5 and 4 K) and the normal state (8 K). The solid lines are fits to Eq. (10), as described in the text. Temperature dependence of the Lorentzian relaxation rate Λ_{ZF} (b) and Gaussian relaxation rate σ_{ZF} (c). The dashed line, which marks the bulk T_c at 5.5 K, is a guide to the eyes. None of the reported fit parameters show distinct anomalies across T_c.

leading to a $\lambda_0 = 141(2)$ nm and to a gap value $\Delta_0 = 1.57k_BT_c = 0.41(1)$ meV.

G. Zero-field μSR

We performed also ZF-μSR measurements, in order to search for a possible TRS breaking in the superconducting state of Mo$_3$P. The large muon gyromagnetic ratio, combined with the availability of 100% spin-polarized muon beams, make ZF-μSR a very sensitive probe for detecting small spontaneous magnetic fields. This technique has been successfully used to detect the TRS breaking in the superconducting states of different types of materials [8,11,12,15,16,50]. Normally, in the absence of external fields, the onset of SC does not imply changes in the ZF muon-spin relaxation rate. However, if the TRS is broken, the onset of tiny spontaneous currents gives rise to associated (weak) magnetic fields, readily detected by ZF-μSR as an increase in muon-spin relaxation rate. Representative ZF-μSR spectra collected above (8 K) and below T_c (1.5 and 4 K) are shown in Fig. 10. For nonmagnetic materials, in the absence of applied fields, the relaxation is mainly determined by the randomly oriented nuclear moments. Consequently, the ZF-μSR spectra of Mo$_3$P could be modeled by means of a combined Lorentzian and Gaussian Kubo-Toyabe relaxation function [51,52]:

$$A_{ZF} = A_s\left[\frac{1}{3} + \frac{2}{3}\left(1 - \sigma_{ZF}^2 t^2 - \Lambda_{ZF}t\right)e^{\left(-\frac{\sigma_{ZF}^2 t^2}{2} - \Lambda_{ZF}t\right)}\right] + A_{bg}.$$

(10)

Here A_s and A_{bg} represent the initial muon-spin asymmetries for muons implanted in the sample and sample holder, respectively. In polycrystalline samples, the 1/3-nonrelaxing and 2/3-relaxing components of the asymmetry correspond to the powder average of the local internal fields with respect to the initial muon-spin orientation. After fixing A_s to its average value of 0.215, the resulting fit parameters are shown in Figs. 10(b) and 10(c). The weak Gaussian and Lorentzian relaxation rates reflect the absence of electronic

magnetic moments and the small value of the Mo$_3$P nuclear moments. Although the ZF-μSR spectra in Fig. 10(a) show tiny differences between the normal and the superconducting state, the resulting $\Lambda_{ZF}(T)$ and $\sigma_{ZF}(T)$ parameters show no distinct changes across T_c. Note that the tiny increase of Λ_{ZF} between the normal and superconducting state [Fig. 10(b)] is not related to a TRS-breaking effect, but to the correlated decrease of σ_{ZF} [Fig. 10(c)]. The clear lack of an additional relaxation below T_c implies that the TRS is preserved in the superconducting state of Mo$_3$P.

H. ^{31}P NMR in the normal phase

NMR is a versatile technique for investigating the electronic properties of materials, in particular, their electron correlations, complementary to μSR with respect to probe location. Considering the rather low T_c and $H_{c2}(0)$ values of Mo$_3$P, as well as the detailed μSR study of its superconducting properties (see previous section), we mostly employed NMR to investigate the normal-state electronic properties of Mo$_3$P. To this aim, ^{31}P NMR measurements were performed at 7 and 0.5 T, i.e., above and below $H_{c2}(0)$ (0.94 T). For both fields, the ^{31}P NMR reference frequency ν_0 was determined by using a solid-state NH$_4$H$_2$PO$_4$ sample, whose Larmor frequency coincides with that of phosphoric acid. The ^{31}P NMR shifts were then calculated with respect to this reference.

Typical ^{31}P NMR line shapes are shown in Fig. 15 in the Appendix. As expected, the NMR lines at 0.5 T show a significant broadening and frequency shift below T_c in the superconducting phase. The 7 T lines, instead, are practically temperature independent, with typical shapes reflecting the Knight shift anisotropy. The Knight shift, peak position, and linewidth were obtained using the DMFIT software [53], with the best-fit parameters being $\delta_{iso} = 285$ ppm, $\Omega = 35$ kHz, and $\eta_{CS} = 0.38$. Here, $\delta_{iso} = (\delta_{11} + \delta_{22} + \delta_{33})/3$ is the isotropic component of the shift tensor, i.e., the average of its diagonal components in the principal-axes system (PAS), the linewidth is $\Omega = |\delta_{11} - \delta_{33}|$, and $\eta_{CS} = (\delta_{22} - \delta_{11})/(\delta_{33} - \delta_{iso})$. The temperature evolution of the linewidths and shifts (normalized to the field value and the reference frequency, respectively) is shown in Fig. 11. The almost temperature- and field-independent linewidths and frequencies suggest a behavior close to that expected for weakly to moderately correlated metals. The above picture changes only close to T_c, below which we detect a significant drop in frequency and increase of linewidth, reflecting the electron pairing and the development of the flux-line lattice in the superconducting phase, respectively. The temperature-dependent NMR relaxation rate $1/T_1$ provides useful insight into the dynamics of conduction electrons and their degree of correlation. The $1/T_1$ data, shown in Fig. 12(a) (inset), indicate an almost linear behavior with slightly different slopes in the regime above and below $T^\star \sim 103$ K. While the change in slope might reflect a change in the electron-nuclei coupling, the linearity of $1/T_1(T)$ is once more a clear indication of weak to moderate electron correlations. This conclusion is confirmed by the $1/T_1T$ data shown in Fig. 12(a) (main panel), where the reported product, at a first approximation considered as constant, is 0.054 s^{-1} K^{-1}. Compared to other metallic superconductors, such as MgB$_2$,
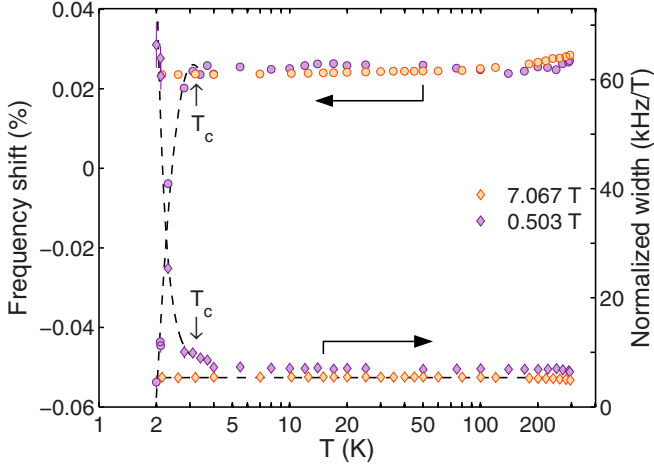
FIG. 11. Normalized ^{31}P NMR Knight shifts $(\delta_{\mathrm{iso}} - \nu_0)/\nu_0$ (left) and linewidths (right) vs temperature, as measured at 0.5 and 7 T. While there is a clear drop of frequency and increase of width below T_c, the data in the normal phase are practically temperature and field independent, indicating an almost ideal metallic behavior.

AlB$_2$, and ZrB$_2$ (see Fig. 5 in Ref. [54]), such a value indicates a good metallicity, i.e., a relatively high electron density of states at the Fermi level. Upon closer inspection we note that, after a minimum at $\sim$20 K, $1/T_1T$ increases slightly with temperature. The origin of this minimum is currently unknown to us.

The Korringa relation [55] states the proportionality between the spin relaxation rate divided by the square of Knight shift (spin part) with the temperature. The total Knight shift K consists of a spin (K_s) and an orbital (K_{orb}) part. Normally these can be separated by using the (typically linear) K-χ plot, with K_{orb} being the intercept value to the K axis. However, as shown in Fig. 16, Mo$_3$P exhibits a complex behavior, most likely reflecting the presence of d-type electrons (see Appendix). In our case, considering the opposite-spin pairing of electrons in the SC phase, we can assume K_s to be fully suppressed at 0 K. From Fig. 11 we can determine $K_{\mathrm{orb}} \sim -0.05\%$ and, hence, $K_s \sim 0.07\%$. Originally derived for simple s-band metals with negligible electronic correlations, K_s was successively extended also to d-band metals, where core polarization effects typically dominate both the Knight shift and the relaxation rate [56]. The experimental value of the proportionality constant and its temperature dependence provide insight into the degree of electron correlations in the normal state of a material. In particular,

$$T_1 T K_s^2 = \alpha S_0, \quad \text{with} \quad S_0 = \frac{\gamma_e^2}{\gamma_N^2} \frac{\hbar}{4\pi k_{\mathrm{B}}}, \qquad (11)$$

where γ_e is the gyromagnetic ratio for a free electron, and γ_N the gyromagnetic ratio of the probe nucleus. Here, α is a coefficient of correlation which, in the ideal case of uncorrelated electrons, should be 1. As shown in Fig. 12(b), in Mo$_3$P the Korringa product is virtually temperature independent (above T_c), since in our case small variations in $1/T_1T$ are mostly compensated by those of the Knight shift (see inset in Fig. 16). The resulting α value is 5.8, i.e., much higher than unity. Since the ^{31}P NMR K_s shift is mostly due to 4d-type
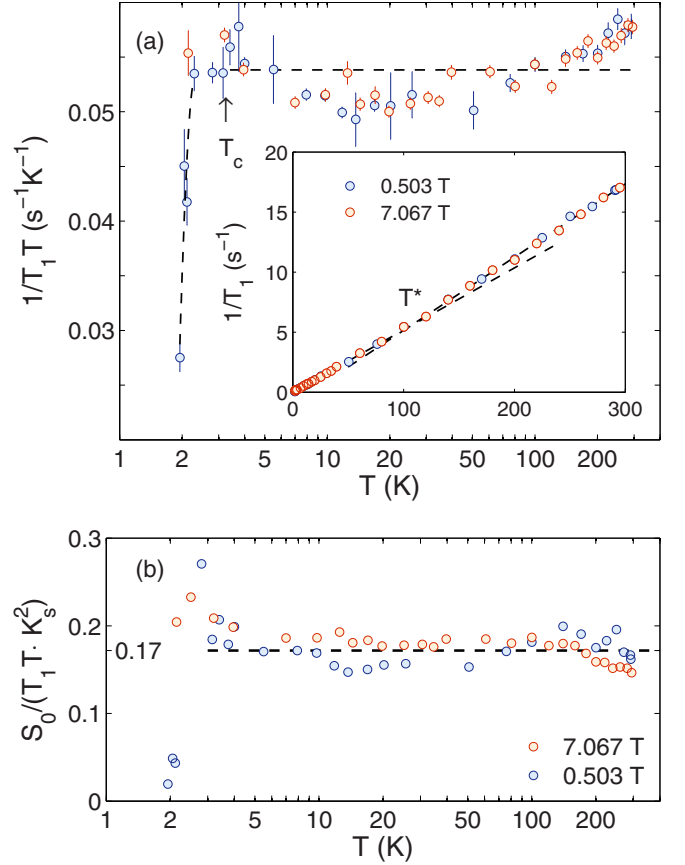

FIG. 12. (a) $1/T_1T$ vs temperature measured at 0.5 and 7 T. Above T_c the product is almost constant (0.054 s^{-1} K^{-1}). Inset: $1/T_1$ vs temperature measured at the same fields. The field-independent spin-lattice relaxation rate is linear in temperature and changes slope at $T^\star \sim 103$ K. (b) The Korringa ratio vs temperature is almost constant down to T_c. An average α^{-1} value much lower than 1 (here shown by a dashed line) suggests ferromagnetic electronic correlations in Mo$_3$P.

conduction electrons (Mo), a high α value is not unusual (see Ref. [57]) and suggests at most moderate ferromagnetic correlations.

I. Electronic band structure and discussion

To further understand the properties of the normal and superconducting states of Mo$_3$P, we performed DFT band-structure calculations, whose main results are summarized in Fig. 13. As shown in panels (a)–(c), close to Fermi level the DOS is dominated by the Mo 4d electrons, while the low-lying states near -6 eV are dominated by contributions from both Mo-4d and P-3p electrons. The estimated DOS at Fermi level is about 1.56 states/(eV f.u.) [= 12.5 states/(eV cell)/Z, with $Z = 8$ the number of Mo$_3$P formula units per unit cell], which is comparable to the experimental results in Sec. III E and Table II. The relatively high DOS hints at a good metallic behavior in Mo$_3$P, confirmed by both electrical resistivity data and the fast NMR relaxation rates. The electronic band structure calculated without considering the SOC is shown in panel (d), while that including SOC in panel (e). In the former case, there are two almost
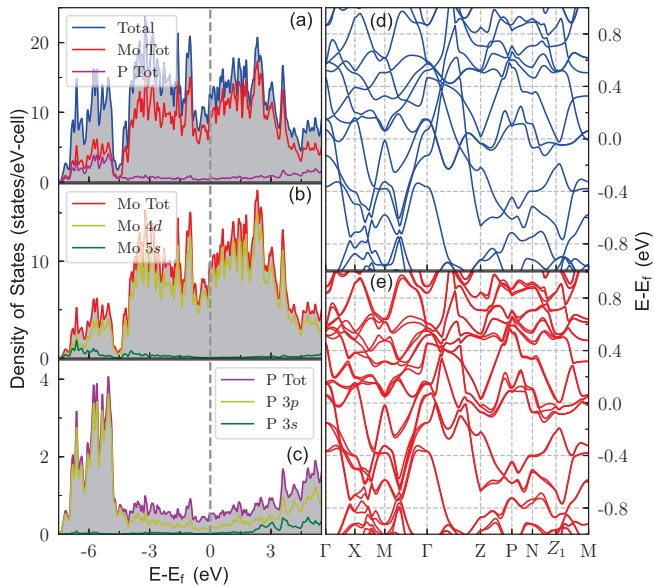
FIG. 13. Calculated electronic band structure for Mo_3P. Total and partial (Mo and P) density of states (a). Orbital-resolved density of states for the Mo (b) and P atoms (c). Band structure of Mo_3P without (d) and with SOC interactions (e), calculated within ± 1 eV from the Fermi energy level.
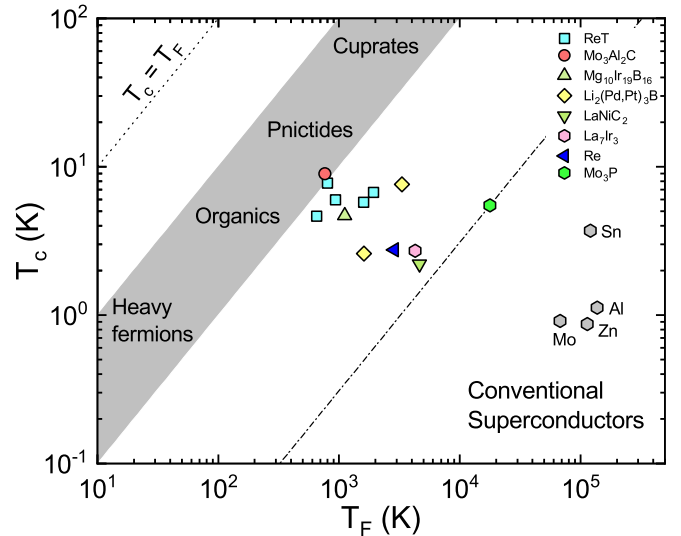

FIG. 14. Uemura plot for different types of superconductors. With $1/100 < T_c/T_F < 1/10$, the gray region indicates the band of unconventional superconductors, including heavy fermions, organics, fullerenes, pnictides, and high-T_c cuprates. Selected noncentrosymmetric and elementary superconductors are shown as symbols (adopted from Refs. [16,65,66]). The dotted line corresponds to $T_c = T_F$ (here T_F is the temperature associated with the Fermi energy, $E_F = k_B T_F$), while the dash-dotted line indicates $T_c/T_F = 3.09 \times 10^{-4}$ for Mo_3P.

overlapping bands at the Z point, about ~ 0.05 eV below the Fermi level. After including the SOC the bands separate, since SOC breaks the band degeneracy and brings one of the bands closer to the Fermi level [see Fig. 13(e)]. The dispersion of the Mo 4d bands, which cross the Fermi level, is rather small with a bandwidth of about ~ 0.3–0.4 eV. The band splitting due to the ASOC is about ~ 90 meV, a value comparable to that of other NCSCs, e.g., Y_2C_3 (~ 15 meV) [58] and $(Sr, Ba)(Ni, Pd)Si_3$ (< 20 meV) [59], but much smaller than that of $CePt_3Si$ (~ 200 meV) [60] and Li_2Pt_3B (~ 200 meV) [61]. It is accepted that the band splitting at Fermi level is of primary importance for the superconducting properties [1]. Indeed, because of the large ASOC-induced band splitting, Li_2Pt_3B shows nodal superconductivity [62], while the upper critical field in $CePt_3Si$ exceeds the Pauli limit [63]. Conversely, in Y_2C_3 and $(Sr, Ba)(Ni, Pd)Si_3$, the upper critical field is relatively small and they are fully gapped superconductors [59,64]. The latter seems also to be the case of Mo_3P, which shows a small band splitting, a low H_{c2} value, and a singlet-pairing superconducting state.

We also compare the superconductivity of Mo_3P with other NCSCs. As shown in Fig. 14, the different families of superconductors can be classified according to the ratio of the superconducting transition temperature T_c to the effective Fermi temperature T_F, in a so-called Uemura plot [66]. Several types of unconventional superconductors, including heavy fermions, organics, high-T_c iron pnictides, and cuprates, all lie in a $1/100 < T_c/T_F < 1/10$ range (gray region). Conversely, conventional BCS superconductors exhibit $T_c/T_F < 1/1000$, here exemplified by the elemental Sn, Al, Zn, and Mo. Most of the NCSCs, e.g., ReT, Mo_3Al_2C, $Li_2(Pd, Pt)_3B$, and $LaNiC_2$, exhibit a T_c/T_F between the unconventional and conventional cases. This is also the case for Mo_3P. According to the super-

conducting parameters obtained from our measurements (see Table II), we find a $T_c/T_F = 3.09 \times 10^{-4}$ for Mo_3P, which is significantly enhanced (~ 30 times) compared to elementary Mo ($T_c/T_F = 0.92/6.77 \times 10^4 = 1.36 \times 10^{-5}$) [41]. On the other hand, Mo_3P shows a similar T_c/T_F value as $LaNiC_2$ and La_7Ir_3 (all lying close to the same dash-dotted line). While the latter exhibit unconventional superconductivity with broken TRS [11,12], the TRS is preserved in Mo_3P. Further studies, such as gap-symmetry analysis, are desirable to offer an answer to such different outcomes.

IV. CONCLUSION

To summarize, we studied the normal- and superconducting-state properties of the Mo_3P NCSC by means of bulk (electrical resistivity, magnetization, and heat capacity) and local-probe (μSR and NMR) techniques and numerical band-structure calculations. The superconducting state of Mo_3P is characterized by $T_c = 5.5$ K, a relatively low $\mu_0 H_{c2}(0) = 0.94$ T, and $\kappa \sim 6$. The temperature dependence of the superfluid density and zero-field electronic specific heat reveal a *nodeless* superconducting state, which is well described by an *isotropic s-wave* model and is consistent with *spin-singlet pairing*. The lack of spontaneous magnetic fields below T_c indicates that time-reversal symmetry is *preserved* in the superconducting state of Mo_3P. Electronic band structure calculations suggest a small band splitting due to the ASOC and a sizable density of states at the Fermi level, confirmed also by NMR, which shows Mo_3P to be a metal with a rather high $N(\epsilon_F)$ and moderate ferromagnetic electron correlations.
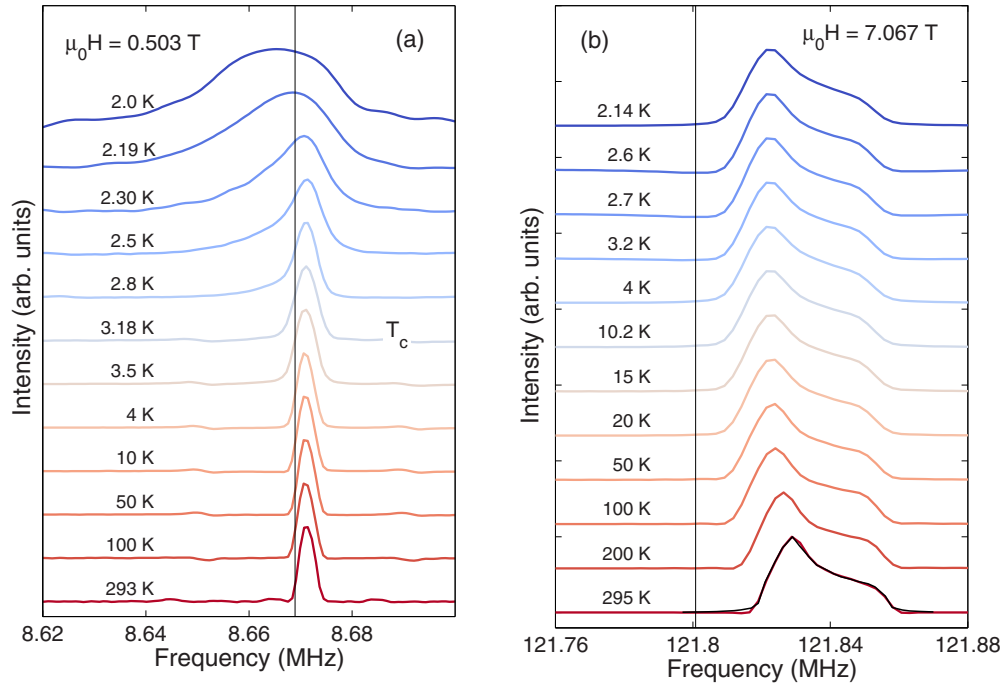
FIG. 15. Selected Mo_3P ^{31}P NMR line shapes measured at (a) 0.5 and (b) 7 T. While at low field a temperature-dependent line broadening and frequency shift are observable (especially below T_c), at high field the line shapes are practically temperature independent. The vertical lines indicate the ^{31}P NMR reference frequencies at the respective fields. The black line on top of the 295 K data in panel (b) represents a fit using a Knight-shift anisotropy model (see text for details).

APPENDIX: NMR LINE SHAPES AND RELAXATION RATES

A selection of ^{31}P NMR line shapes for both magnetic fields (0.5 and 7 T) is shown in Fig. 15. At low field (a), the transition to the superconducting phase at low temperature is indicated by a broadening of the line and by its qualitative change of shape. Above T_c, the line shape is described by a Gaussian (analysis performed by DMFIT), whereas below T_c, the line shapes can be fitted by means of a convolution of a Gaussian with a Lorentzian. At high field (b), the SC phase transition is suppressed by the applied magnetic field, which also enhances the anisotropy of the line shapes. The black line on top of the 295 K data represents a fit using a Knight-shift anisotropy model (see main text). Here, $\delta_{11} > \delta_{22} > \delta_{33}$ represent the principal components of the shift tensor, identified with the shoulders and the maximum (δ_{22}) of the NMR line shapes shown in Fig. 15(b). The fit parameters in the Herzfeld-Berger notation [67] used here are the isotropic component of the shift tensor δ_{iso} (i.e., the trace average), the linewidth Ω, and the anisotropy η_{CS} (see main text).

The Clogston-Jaccarino K-χ plot shown in Fig. 16 clearly indicates that the Knight shift depends linearly on the molar susceptibility χ in the range $(0.5\text{–}1) \times 10^{-4}$ emu/mol, corresponding to a temperature range 2–50 K. This linear dependency is given by

$$K(\chi)\,[\%] = -1.6451 \times 10^{-3}\chi + 2.5226 \times 10^{-2}. \quad (A1)$$
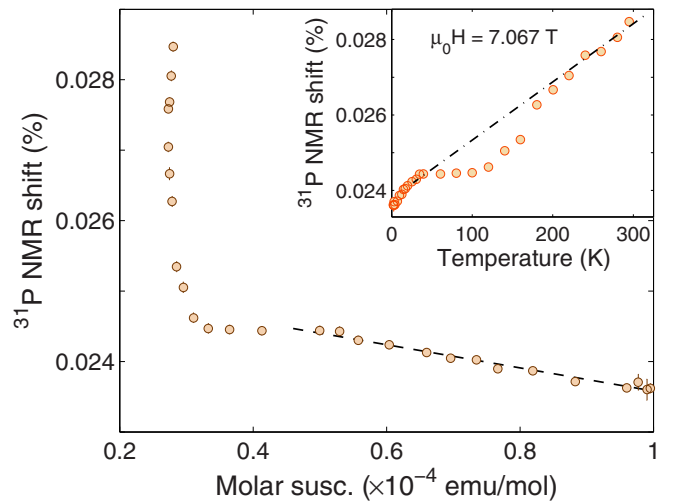

FIG. 16. Clogston-Jaccarino K-χ plot for Mo_3P as measured at 7.067 T. The low-temperature part was fitted by using a linear relation, as given in Eq. (A1). Inset: ^{31}P NMR shift vs temperature measured at the same field. The dash-dotted line highlights the shift deviations in the 50–200 K range.

The offset may indicate the presence of other temperature-independent components. The coupling constant [i.e., the coefficient in Eq. (A1)] may become temperature dependent for $\chi < 0.5 \times 10^{-4}$ emu/mol [68]. From the slope $dK/d\chi$ of the K-χ plot for $T < 50$ K, by assuming a standard electronic g factor of 2.0, the relation $K = gA_{hf}\chi + K_{offset}$ gives a hyperfine coupling constant $A_{hf} = -0.082$ T/μ_B and a zero intercept of 0.025%.

As shown in Fig. 16, both the K-χ plot behavior and the temperature dependence of the NMR shift are rather complicated. This is not unusual for d-type electron systems, known for their nonlinear $K(T)$ dependencies (see, e.g., Ref. [69]). In our case, between approximately 30 and 200 K, the Knight shift deviates markedly from linearity to exhibit a shallow minimum around 100 K. At 30 K, $1/(T_1 T)$ exhibits a minimum [see Fig. 12(a)], while around 100 K, $1/T_1$ changes slope. Since these anomalies appear in rather independent types of measurements (K and T_1), they might represent true modifications of the Mo_3P electronic properties. Although currently an explanation concerning their nature is missing, future studies of the Hall coefficient vs temperature might help to better determine their origin.

[1] E. Bauer and M. Sigrist, editors, *Non-Centrosymmetric Superconductors*, Lecture Notes in Physics (Springer, Berlin, 2012), Vol. 847.

[2] M. Smidman, M. B. Salamon, H. Q. Yuan, and D. F. Agterberg, Superconductivity and spin-orbit coupling in noncentrosymmetric materials: A review, Rep. Prog. Phys. **80**, 036501 (2017).

[3] K. Ishida, H. Mukuda, Y. Kitaoka, K. Asayama, Z. Q. Mao, Y. Mori, and Y. Maeno, Spin-triplet superconductivity in Sr_2RuO_4 identified by ^{17}O Knight shift, Nature (London) **396**, 658 (1998).

[4] H. Tou, Y. Kitaoka, K. Ishida, K. Asayama, N. Kimura, Y. Ōnuki, E. Yamamoto, Y. Haga, and K. Maezawa, Nonunitary Spin-Triplet Superconductivity in UPt_3: Evidence from ^{195}Pt Knight Shift Study, Phys. Rev. Lett. **80**, 3129 (1998).

[5] A. Mackenzie and Y. Maeno, The superconductivity of Sr_2RuO_4 and the physics of spin-triplet pairing, Rev. Mod. Phys. **75**, 657 (2003), and references therein.

[6] R. Joynt and L. Taillefer, The superconducting phases of UPt_3, Rev. Mod. Phys. **74**, 235 (2002), and references therein.

[7] G. M. Luke, A. Keren, L. P. Le, W. D. Wu, Y. J. Uemura, D. A. Bonn, L. Taillefer, and J. D. Garrett, Muon Spin Relaxation in UPt_3, Phys. Rev. Lett. **71**, 1466 (1993).

[8] G. M. Luke, Y. Fudamoto, K. M. Kojima, M. I. Larkin, J. Merrin, B. Nachumi, Y. J. Uemura, Y. Maeno, Z. Q. Mao, Y. Mori, H. Nakamura, and M. Sigrist, Time-reversal symmetry-breaking superconductivity in Sr_2RuO_4, Nature (London) **394**, 558 (1998).

[9] J. Xia, Y. Maeno, P. T. Beyersdorf, M. M. Fejer, and A. Kapitulnik, High Resolution Polar Kerr Effect Measurements of Sr_2RuO_4: Evidence for Broken Time-Reversal Symmetry in the Superconducting State, Phys. Rev. Lett. **97**, 167002 (2006).

[10] E. R. Schemm, W. J. Gannon, C. M. Wishne, W. P. Halperin, and A. Kapitulnik, Observation of broken time-reversal symmetry in the heavy-fermion superconductor UPt_3, Science **345**, 190 (2014).

[11] A. D. Hillier, J. Quintanilla, and R. Cywinski, Evidence for Time-Reversal Symmetry Breaking in the Noncentrosymmetric Superconductor $LaNiC_2$, Phys. Rev. Lett. **102**, 117007 (2009).

[12] J. A. T. Barker, D. Singh, A. Thamizhavel, A. D. Hillier, M. R. Lees, G. Balakrishnan, D. M. Paul, and R. P. Singh, Unconventional Superconductivity in La_7Ir_3 Revealed by Muon Spin Relaxation: Introducing a New Family of Noncentrosymmetric Superconductor that Breaks Time-Reversal Symmetry, Phys. Rev. Lett. **115**, 267001 (2015).

[13] R. P. Singh, A. D. Hillier, B. Mazidian, J. Quintanilla, J. F. Annett, D. M. Paul, G. Balakrishnan, and M. R. Lees, Detection of Time-Reversal Symmetry Breaking in the Noncentrosymmetric Superconductor Re_6Zr Using Muon-Spin Spectroscopy, Phys. Rev. Lett. **112**, 107002 (2014).

[14] D. Singh, J. A. T. Barker, A. Thamizhavel, D. M. Paul, A. D. Hillier, and R. P. Singh, Time-reversal symmetry breaking in the noncentrosymmetric superconductor Re_6Hf: Further evidence for unconventional behavior in the α-Mn family of materials, Phys. Rev. B **96**, 180501(R) (2017).

[15] T. Shang, G. M. Pang, C. Baines, W. B. Jiang, W. Xie, A. Wang, M. Medarde, E. Pomjakushina, M. Shi, J. Mesot, H. Q. Yuan, and T. Shiroka, Nodeless superconductivity and time-reversal symmetry breaking in the noncentrosymmetric superconductor $Re_{24}Ti$, Phys. Rev. B **97**, 020502(R) (2018).

[16] T. Shang, M. Smidman, S. K. Ghosh, C. Baines, L. J. Chang, D. J. Gawryluk, J. A. T. Barker, R. P. Singh, D. M. Paul, G. Balakrishnan, E. Pomjakushina, M. Shi, M. Medarde, A. D. Hillier, H. Q. Yuan, J. Quintanilla, J. Mesot, and T. Shiroka, Time-Reversal Symmetry Breaking in Re-Based Superconductors, Phys. Rev. Lett. **121**, 257002 (2018).

[17] J. Quintanilla, A. D. Hillier, J. F. Annett, and R. Cywinski, Relativistic analysis of the pairing symmetry of the noncentrosymmetric superconductor $LaNiC_2$, Phys. Rev. B **82**, 174511 (2010).

[18] A. D. Hillier, J. Quintanilla, B. Mazidian, J. F. Annett, and R. Cywinski, Nonunitary Triplet Pairing in the Centrosymmetric Superconductor $LaNiGa_2$, Phys. Rev. Lett. **109**, 097001 (2012).

[19] Z. F. Weng, J. L. Zhang, M. Smidman, T. Shang, J. Quintanilla, J. F. Annett, M. Nicklas, G. M. Pang, L. Jiao, W. B. Jiang, Y. Chen, F. Steglich, and H. Q. Yuan, Two-Gap Superconductivity in $LaNiGa_2$ with Nonunitary Triplet Pairing and Even Parity Gap Symmetry, Phys. Rev. Lett. **117**, 027001 (2016).

[20] S. Ghosh, J. F. Annett, and J. Quintanilla, Time-reversal symmetry breaking in superconductors through loop Josephson-current order, arXiv:1803.02618.

[21] B. T. Matthias, E. Corenzwit, and C. E. Miller, Superconducting compounds, Phys. Rev. **93**, 1415 (1954).

[22] R. D. Blaugher, J. K. Hulm, and P. N. Yocom, Superconducting phosphides of the transition metals, J. Phys. Chem. Solids **26**, 2037 (1965).

[23] B. Sellberg and S. Rundqvist, The crystal structure of Mo_3P, Acta Chem. Scand. **19**, 760 (1965).

[24] A. Amato, H. Luetkens, K. Sedlak, A. Stoykov, R. Scheuermann, M. Elender, A. Raselli, and D. Graf, The new versatile general purpose surface-muon instrument (GPS) based on silicon photomultipliers for μSR measurements on a continuous-wave beam, Rev. Sci. Instrum. **88**, 093301 (2017).

[25] A. A. Suter and B. M. Wojek, Musrfit: A free platform-independent framework for μ SR data analysis, Phys. Procedia **30**, 69 (2012).

[26] P. Blaha, K. Schwarz, G. K. H. Madsen, D. Kvasnicka, and J. Luitz, *WIEN2k, An Augmented Plane Wave + Local Orbitals Program for Calculating Crystal Properties* (Karlheinz Schwarz, Techn. Universität Wien, Austria, 2001).

[27] J. P. Perdew, K. Burke, and M. Ernzerhof, Generalized Gradient Approximation Made Simple, Phys. Rev. Lett. **77**, 3865 (1996).

[28] J. Rodríguez-Carvajal, Recent advances in magnetic structure determination by neutron powder diffraction, Physica B (Amsterdam) **192**, 55 (1993).

[29] F. Bloch, Zum elektrischen Widerstandsgesetz bei tiefen Temperaturen, Z. Phys. **59**, 208 (1930).

[30] F. J. Blatt, *Physics of Electronic Conduction in Solids* (McGraw-Hill, New York, 1968), pp. 185–190.

[31] N. F. Mott and H. Jones, *The Theory of the Properties of Metals and Alloys* (Oxford University Press, London, 1958).

[32] N. F. Mott, Electrons in transition metals, Adv. Phys. **13**, 325 (1964).

[33] X. Zhu, H. Yang, L. Fang, G. Mu, and H.-H. Wen, Upper critical field, Hall effect and magnetoresistance in the iron-based layered superconductor $LaFeAsO_{0.9}F_{0.1-\delta}$, Supercond. Sci. Technol. **21**, 105001 (2008).

[34] N. R. Werthamer, E. Helfand, and P. C. Hohenberg, Temperature and purity dependence of the superconducting critical field, H_{c2}. III. Electron spin and spin-orbit effects, Phys. Rev. **147**, 295 (1966).

[35] F. Kneidinger, H. Michor, A. Sidorenko, E. Bauer, I. Zeiringer, P. Rogl, C. Blaas-Schenner, D. Reith, and R. Podloucky, Synthesis, characterization, electronic structure, and phonon properties of the noncentrosymmetric superconductor LaPtSi, Phys. Rev. B **88**, 104508 (2013).

[36] D. C. Peets, A. Maldonado, M. Enayat, Z. Sun, P. Wahl, and A. P. Schnyder, Upper critical field of the noncentrosymmetric superconductor BiPd, Phys. Rev. B **93**, 174504 (2016).

[37] N. Kimura, N. Kabeya, K. Saitoh, K. Satoh, H. Ogi, K. Ohsaki, and H. Aoki, Type II/1 superconductivity with extremely high H_{c3} in noncentrosymmetric $LaRhSi_3$, J. Phys. Soc. Jpn. **85**, 024715 (2016).

[38] V. K. Anand, D. Britz, A. Bhattacharyya, D. T. Adroja, A. D. Hillier, A. M. Strydom, W. Kockelmann, B. D. Rainford, and K. A. McEwen, Physical properties of noncentrosymmetric superconductor $LaIrSi_3$: A μSR study, Phys. Rev. B **90**, 014513 (2014).

[39] M. Smidman, A. D. Hillier, D. T. Adroja, M. R. Lees, V. K. Anand, R. P. Singh, R. I. Smith, D. M. Paul, and G. Balakrishnan, Investigations of the superconducting states of noncentrosymmetric $LaPdSi_3$ and $LaPtSi_3$, Phys. Rev. B **89**, 094509 (2014).

[40] E. H. Brandt, Properties of the ideal Ginzburg-Landau vortex lattice, Phys. Rev. B **68**, 054506 (2003).

[41] C. Kittel, *Introduction to Solid State Physics*, 8th ed. (John Wiley & Sons, Hoboken, NJ, 2005).

[42] W. L. McMillan, Transition temperature of strong-coupled superconductors, Phys. Rev. **167**, 331 (1968).

[43] R. I. Boughton, J. L. Olsen, and C. Palmy, Pressure effects in superconductors, in Prog. Low Temp. Phys. **6**, 163 (1970).

[44] T. Shang, D. J. Gawryluk, J. A. T. Verezhak, E. Pomjakushina, M. Shi, M. Medarde, J. Mesot, and T. Shiroka, Structure and superconductivity in the binary $Re_{1-x}Mo_x$ alloys, Phys. Rev. Mater. **3**, 024801 (2019).

[45] M. Tinkham, *Introduction to Superconductivity*, 2nd ed. (Dover Publications, Mineola, NY, 1996).

[46] H. Padamsee, J. E. Neighbor, and C. A. Shiffman, Quasiparticle phenomenology for thermodynamics of strong-coupling superconductor, J. Low Temp. Phys. **12**, 387 (1973).

[47] A. Maisuradze, R. Khasanov, A. Shengelaya, and H. Keller, Comparison of different methods for analyzing μSR line shapes in the vortex state of type-II superconductors, J. Phys.: Condens. Matter **21**, 075701 (2009), and references therein.

[48] W. Barford and J. M. F. Gunn, The theory of the measurement of the London penetration depth in uniaxial type II superconductors by muon spin rotation, Phys. C (Amsterdam) **156**, 515 (1988).

[49] A. Carrington and F. Manzano, Magnetic penetration depth of MgB_2, Physica C (Amsterdam) **385**, 205 (2003).

[50] Y. Aoki, A. Tsuchiya, T. Kanayama, S. R. Saha, H. Sugawara, H. Sato, W. Higemoto, A. Koda, K. Ohishi, K. Nishiyama, and R. Kadono, Time-Reversal Symmetry-Breaking Superconductivity in Heavy-Fermion $PrOs_4Sb_{12}$ detected by muon-spin relaxation, Phys. Rev. Lett. **91**, 067003 (2003).

[51] R. Kubo and T. Toyabe, A stochastic model for low field resonance and relaxation, in *Magnetic Resonance and Relaxation*, edited by R. Blinc (North-Holland, Amsterdam, 1967), pp. 810–823.

[52] A. Yaouanc and P. D. de Réotier, *Muon Spin Rotation, Relaxation, and Resonance: Applications to Condensed Matter* (Oxford University Press, Oxford, 2011).

[53] D. Massiot, F. Fayon, M. Capron, I. King, S. Le Calvé, B. Alonso, J.-O. Durand, B. Bujoli, Z. Gan, and G. Hoatson, Modelling one- and two-dimensional solid-state NMR spectra, Magn. Reson. Chem. **40**, 70 (2002).

[54] N. Barbero, T. Shiroka, B. Delley, T. Grant, A. J. S. Machado, Z. Fisk, H.-R. Ott, and J. Mesot, Doping-induced superconductivity of ZrB_2 and HfB_2, Phys. Rev. B **95**, 094505 (2017).

[55] J. Korringa, Nuclear magnetic relaxation and resonance line shift in metals, Physica (Amsterdam) **16**, 601 (1950).

[56] Y. Yafet and V. Jaccarino, Nuclear spin relaxation in transition metals; core polarization, Phys. Rev. **133**, A1630 (1964).

[57] A. Narath and H. T. Weaver, Effects of electron-electron interactions on nuclear spin-lattice relaxation rates and Knight shifts in alkali and noble metals, Phys. Rev. **175**, 373 (1968).

[58] Y. Nishikayama, T. Shishidou, and T. Oguchi, Electronic properties of Y_2C_3 by first-principles calculations, J. Phys. Soc. Jpn. **76**, 064714 (2007).

[59] F. Kneidinger, L. Salamakha, E. Bauer, I. Zeiringer, P. Rogl, C. Blaas-Schenner, D. Reith, and R. Podloucky, Superconductivity in noncentrosymmetric $BaAl_4$ derived structures, Phys. Rev. B **90**, 024504 (2014).

[60] K. V. Samokhin, E. S. Zijlstra, and S. K. Bose, $CePt_3Si$: An unconventional superconductor without inversion center, Phys. Rev. B **69**, 094514 (2004).

[61] K.-W. Lee and W. E. Pickett, Crystal symmetry, electron-phonon coupling, and superconducting tendencies in Li$_2$Pd$_3$B and Li$_2$Pt$_3$B, Phys. Rev. B **72**, 174505 (2005).

[62] H. Q. Yuan, D. F. Agterberg, N. Hayashi, P. Badica, D. Vandervelde, K. Togano, M. Sigrist, and M. B. Salamon, *S*-Wave Spin-Triplet Order in Superconductors without Inversion Symmetry: Li$_2$Pd$_3$B and Li$_2$Pt$_3$B, Phys. Rev. Lett. **97**, 017006 (2006).

[63] E. Bauer, G. Hilscher, H. Michor, C. Paul, E. W. Scheidt, A. Gribanov, Y. Seropegin, H. Noël, M. Sigrist, and P. Rogl, Heavy Fermion Superconductivity and Magnetic Order in Noncentrosymmetric CePt$_3$Si, Phys. Rev. Lett. **92**, 027003 (2004).

[64] S. Kuroiwa, Y. Saura, J. Akimitsu, M. Hiraishi, M. Miyazaki, K. H. Satoh, S. Takeshita, and R. Kadono, Multigap Superconductivity in Sesquicarbides La$_2$C$_3$ and Y$_2$C$_3$, Phys. Rev. Lett. **100**, 097002 (2008).

[65] J. A. T. Barker, B. D. Breen, R. Hanson, A. D. Hillier, M. R. Lees, G. Balakrishnan, D. M. Paul, and R. P. Singh, Superconducting and normal-state properties of the noncentrosymmetric superconductor Re$_3$Ta, Phys. Rev. B **98**, 104506 (2018), and references therein.

[66] Y. J. Uemura, L. P. Le, G. M. Luke, B. J. Sternlieb, W. D. Wu, J. H. Brewer, T. M. Riseman, C. L. Seaman, M. B. Maple, M. Ishikawa, D. G. Hinks, J. D. Jorgensen, G. Saito, and H. Yamochi, Basic Similarities among Cuprate, Bismuthate, Organic, Chevrel-Phase, and Heavy-Fermion Superconductors Shown by Penetration-Depth Measurements, Phys. Rev. Lett. **66**, 2665 (1991).

[67] J. Herzfeld and A. E. Berger, Sideband intensities in NMR spectra of samples spinning at the magic angle, J. Chem. Phys. **73**, 6021 (1980).

[68] P.-C. Ho, D. E. MacLaughlin, L. Shu, O. O. Bernal, S. Zhao, A. A. Dooraghi, T. Yanagisawa, M. B. Maple, and R. H. Fukuda, Muon spin rotation and relaxation in Pr$_{1-x}$Nd$_x$Os$_4$Sb$_{12}$: Paramagnetic states, Phys. Rev. B **89**, 235111 (2014).

[69] G. S. Carter, L. H. Bennett, and D. J. Kahan, *Metallic Shifts in NMR* (Pergamon Press, Oxford, 1977).